Topological Dirac semimetal BaAuSb

Zhixiang Hu (胡之翔),[1,2] Jahyun Koo,[3] Yong Hu (胡勇),[4] Qi Wang (王琦),[1,5,*] Milinda Abeykoon,[6] D. Graf,[7] Yu Liu (刘育),[1,†] Hechang Lei (雷和畅),[5] Junzhang Ma (馬均章),[8] Ming Shi (史明),[4] Binghai Yan (颜丙海),[3,‡] and C. Petrovic[1,2,§]

[1]*Condensed Matter Physics and Materials Science Department, Brookhaven National Laboratory, Upton, New York 11973, USA*
[2]*Department of Material Science and Chemical Engineering, Stony Brook University, Stony Brook, New York 11790, USA*
[3]*Department of Condensed Matter Physics, Weizmann Institute of Science, Rehovot 7610001, Israel*
[4]*Photon Science Division, Paul Scherrer Institut, CH-5232 Villigen PSI, Switzerland*
[5]*Department of Physics and Beijing Key Laboratory of Opto-electronic Functional Materials & Micro-nano Devices, Renmin University of China, Beijing 100872, China*
[6]*Photon Science Division, National Synchrotron Light Source II, Brookhaven National Laboratory, Upton, New York 11973, USA*
[7]*National High Magnetic Field Laboratory, Florida State University, Tallahassee, Florida 32306-4005, USA*
[8]*Department of Physics, City University of Hong Kong, Kowloon, Hong Kong, China*

(Received 5 September 2022; revised 9 January 2023; accepted 11 January 2023; published 3 February 2023)

Dirac semimetals feature Dirac cones with topologically nontrivial states in the bulk that are protected by crystalline symmetries. They attract considerable attention due to rich quantum states and properties of interest, such as high Fermi velocities, mobility, and small effective masses. Here, we show that a ternary intermetallic BaAuSb crystal hosts both trivial and nontrivial topological Dirac states in the bulk. The nontrivial Fermi-surface pocket at the Brillouin zone center is characterized with only a few hundredths of a bare electron mass and with very high mobility. All parts of the Fermi surface detected by quantum oscillations, topologically trivial or nontrivial, have carriers with unusually high Fermi velocities and small masses. These conducting states may be coupled with magnetic moments in materials where Ba is replaced by magnetic rare-earth atoms.

DOI: 10.1103/PhysRevResearch.5.013079

I. INTRODUCTION

Topological Dirac semimetals (TDSMs) are of high current interest. In contrast to normal semimetals, their charge carriers obey a Dirac equation, i.e., energies linearly dispersing in momentum space at the Dirac node. Due to spin-orbit coupling (SOC), there is spin momentum locking where the spin orientation is constrained perpendicularly to the electron momentum. Suppressed backscattering contributes to a very high carrier mobility and in addition many exotic quantum states emerge [1–7].

Heavy element compounds with high symmetries are a fertile ground to search for new Dirac semimetals due to a strong SOC interaction proportional to Z^4, where Z is the atomic number [8,9]. SOC induces a gap in the overlapping valence and conduction bands by removing multiple irreducible representations of the space group Ψ_i in a Hamiltonian matrix, mathematically expressed as $\langle E_n, \Psi_i | V | E_m, \Psi_i \rangle$, in which $E_{n,m}$ presents the associated energy and V is the periodic potential inside the crystal. Crystalline symmetries protect touching spots and Dirac cones appear at the high-symmetry points in the Brillouin zone [9].

BaAuSb crystallizes in a hexagonal crystal lattice with space group $P6_3/mmc$ (194) [Fig. 1(a)], is a part of the ABX family (A = alkaline earth, B = transition metal, X = pnictogen), and shares the same crystal structure with the topological Dirac semimetal CaAuAs that features dominant hole-type carriers with both three-dimensional (3D) and quasi-two-dimensional (2D) Fermi-surface sheets [10–12]. BaAuSb is predicted to be a charge-balanced TDSM where a Dirac cone arises in the Γ-A direction from band crossing with a different symmetry representation in the bulk band structure [13,14]. Here, we present insight into the Fermi-surface characteristics of BaAuSb via combined quantum oscillation, angular-resolved photoemission (ARPES), and first-principles calculation studies. Our results indicate small effective masses and a compensated nature of the electronic structure near the Fermi level. We present evidence that some Fermi-surface sheets are nontrivial and 3D, but all detected Fermi-surface pockets feature relatively large Fermi velocities. The topologically nontrivial electronic states have an exceedingly small

*Present address: School of Physical Science and Technology, Shanghai Tech University, Shanghai 201210, China.
†Present address: Los Alamos National Laboratory, MS K764, Los Alamos, New Mexico 87545, USA.
‡binghai.yan@weizmann.ac.il
§petrovic@bnl.gov

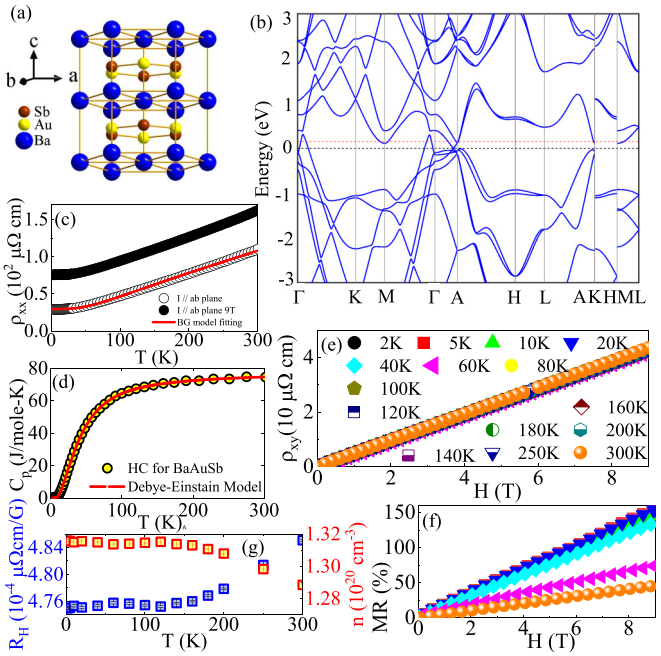

FIG. 1. (a) Crystal structure and (b) band structure of BaAuSb depicted with spin-orbit coupling and a Fermi-level shift that matches the experimental results (see text). (c) Electric resistivity of BaAuSb measured for current flow in the *ab* plane and Bloch-Grüneisen model fit. (d) Heat capacity of BaAuSb with an Einstein-Debye model fit. (e) Hall resistivity and (f) transverse magnetoresistance (MR $= [\rho(B) - \rho(0)]/\rho(0) \times 100\%$) of BaAuSb. (g) Hall coefficient R_H and carrier density n as a function of temperature.

mass, of the order of $1/100$ of the bare electron mass. Our results point to possible spin polarization in BaAuSb-type materials where Ba is replaced by divalent magnetic rare-earth atoms.

II. RESULTS AND DISCUSSION

The unit cell can be viewed as stacks of Ba honeycombs along the hexagonal c axis, which maintain bulk inversion symmetries [Fig. 1(a)]. Between two layers of Ba, there are Au-Sb hexagonal rings, similar to CaAuAs. In isostructural BaAgBi, SOC gaps all states except along the Γ-A direction, leading to a 3D TDSM state with two Dirac points due to symmetry [13]. The band structure of BaAuSb [Fig. 1(b)] features Dirac-like points around Γ, in the Γ-A and Γ-K directions in the Brillouin zone in the vicinity of Fermi energy, as in KZnBi, and implying a 3D character of the bulk bands due to significant dispersion along k_z [15]. The main effect of SOC is to shift the Dirac point in the Γ-A direction to the Fermi level [15].

Electric resistivity [Fig. 1(c)] is metallic. In the absence of magnetic field it could be explained by the dominant phonon scattering via the Bloch-Grüneisen formula,

$$\rho(T) = \rho_0 + A\left(\frac{T}{\theta_D}\right)^5 \int_0^{\frac{\theta_D}{T}} \frac{z^5}{(e^z - 1)(1 - e^{-z})} dz, \qquad (1)$$

where $\theta_D = 372(7)$ K is the Debye temperature. Application of a 9 T magnetic field brings no significant change except for a uniform increase in resistivity values as observed in other compensated semimetals in the absence of a field-induced gap at the contact point of the Dirac bands [16–18]. The heat capacity [Fig. 1(d)] is fitted by the Einstein-Debye model [19,20],

$$C_{\text{el+ph}}(T) = \gamma T + (1 - \alpha)9nR\left(\frac{T}{\theta_D}\right)^3 \int_0^{\frac{\theta_D}{T}} \frac{x^4 e^x}{(e^x - 1)^2} dx + \alpha 3nR \frac{(\theta_E/T)^2 e^{\theta_E/T}}{(e^{\theta_E/T} - 1)^2}, \qquad (2)$$

where N is the atomic number, α is the number of Einstein modes, and R is the universal gas constant. The fit gives $\alpha = 0.37(2)$, $\gamma = 7(1)$ mJ/mol K^2, Debye temperature $\Theta_D = 208(3)$ K, and Einstein temperature $\Theta_E = 79(1)$ K. This indicates that in phonon-related $\rho(T)$ scattering involves both acoustic and optical phonon modes and that the heat capacity cannot be simply approximated as a linear dispersion of acoustic modes where the phonon density of states is zero above the cutoff temperature θ_D. This could arise due to a significant number of weakly bound independent oscillators (e.g., Ba) in a Debye bath (Au-Sb hexagonal rings), similar to hexaborides where rare-earth atoms show an independent contribution to heat capacity from the rigid boron sublattice [21,22].

Hall resistivity ρ_{xy} [Fig. 1(e)] and unsaturated transverse magnetoresistance (MR) [Fig. 1(f)] point out that a single band is dominant in the electronic transport. The linear resistivity ρ_{xy} in magnetic field gives temperature-dependent Hall coefficients R_H estimated from the slopes of ρ_{xy} vs H [Fig. 1(h)]. Carrier densities n at different temperatures are calculated from $R_H = \frac{1}{ne}$, where e is the electronic charge. The carrier density shows a steady plateau at lower temperature and a linear reduction above 150 K [Fig. 1(g)].

Angle-dependent de Haas–van Alphen (dHvA) responses of high frequencies oscillate for all angles [Fig. 2(a)]. Experiments were performed with a rotator where the crystal was rotated and the angle between the magnetic field direction and crystalline c axis (θ) are depicted in Fig. 2(a) inset. Figures 2(b) and 2(c) plot the fast Fourier transform (FFT) to the dHvA response. Three frequencies are seen, α, β, and γ. The frequencies are plotted separately due to the large differences between them. Offsets are added to FFT responses so that a trace of evolutions for frequencies α [Fig. 2(b)] and β, γ [Fig. 2(c)] are clearly seen as a function of angle where $F_\alpha = 5(1)$ T, and $F_\beta = 305(2)$ T, $F_\gamma = 358(2)$ T at $\theta = 0$. Frequencies indicate three Fermi-surface pockets in the reciprocal space of BaAuSb. Frequencies β, γ show a similar evolution with an angle up to 90°, though the magnitude of frequency γ is somewhat larger. Over 90°, both frequencies are reduced.

The changes with angle for all frequencies could be fitted by the ellipsoidal model [Figs. 2(d) and 2(e)],

$$F(\theta) = \frac{A}{\sqrt{\epsilon^2 \sin^2(\theta + \phi) + \cos^2(\theta + \phi)}}, \qquad (3)$$

where ϵ is the ellipse eccentricity; ϕ is a phase, indicating that all detected Fermi surfaces (FSs) of BaAuSb are 3D. From the Onsager relation where e is the elemental charge and $\hbar$ is Planck's constant, $F = (c\hbar/2\pi e)S_F$, we calculate the ex-

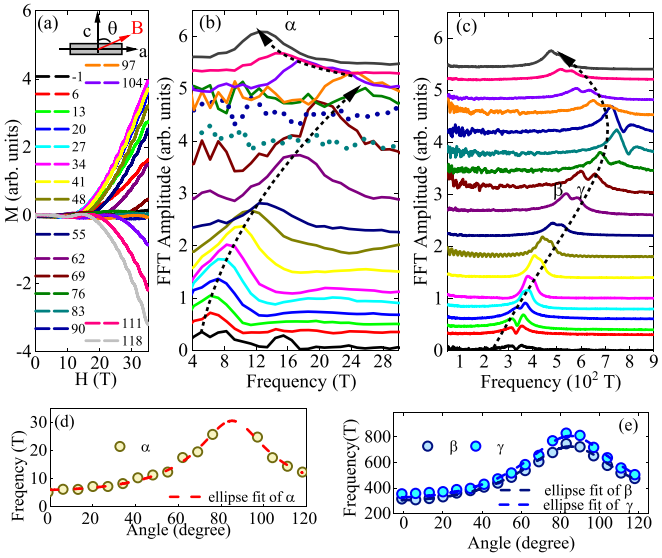

FIG. 2. (a) Angle-dependent dHvA oscillations. The BaAuSb crystal installed on a cantilever is rotated from -1° to 118° with data collected approximately every 7°. (b), (c) FFT of low frequency α and of high frequencies β, γ. FFT is taken from ΔM, where $\Delta M = M - \langle M \rangle$, and $\langle M \rangle$ is the background. The α frequency increases before reaching 90°, and reduces for higher angles. Two high frequencies evolve similarly and arrive at their maximum around 90°. (d) The 3D model is applied to low frequency α; responses after 90° are translated to a negative angle for clarity. (e) The 3D model is applied to high frequencies β and γ.

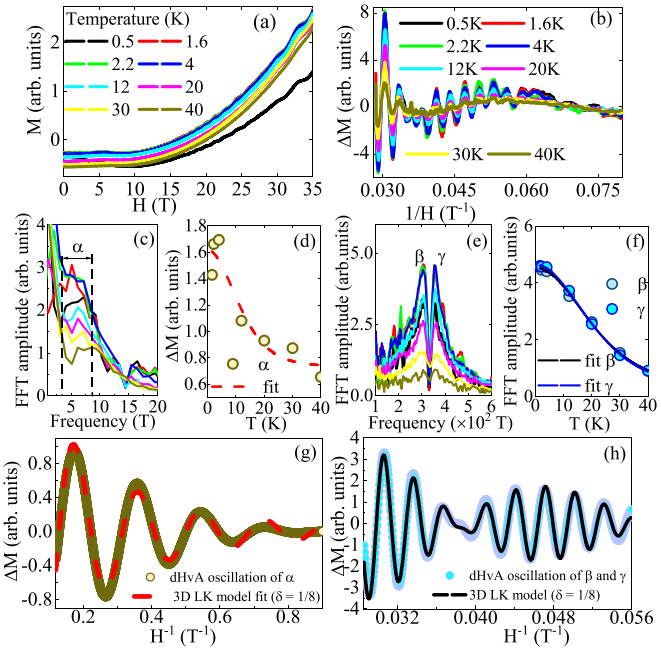

FIG. 3. (a) Temperature-dependent dHvA oscillations of BaAuSb. (b) Background-free dHvA response ΔM vs $1/H$ with $\Delta M = M - \langle M \rangle$. (c), (d) Effective mass on a Fermi sheet of α is estimated by the temperature factor in the Lifshitz-Kosevich (LK) formula. (e), (f) Effective mass on a Fermi sheet of β, γ is estimated by the temperature factor in the LK formula. (g) 2D LK formula applied to fit low frequency α at 1.6 K. Solid lines represent the 2D LK formula fit. (h) 3D LK formula applied to fit oscillations for high frequencies β and γ at 1.6 K. Solid lines represent the 3D LK formula fit.

tremal Fermi-surface area S_F associated with the α, β, and γ pockets to be $5(1) \times 10^{-2}$ nm^{-2}, $2.91(2)$ nm^{-2} $= 2.91(2) \times 10^{-2}$ Å^{-2} and $3.41(2)$ nm^{-2} $= 3.41(2) \times 10^{-2}$ Å^{-2}, respectively. We also calculate Fermi velocities $v_{F\alpha} = 2.1(2) \times 10^5$ m/s, $v_{F\beta} = 1.01(5) \times 10^6$ m/s, $v_{F\gamma} = 1.08(3) \times 10^6$ m/s, and Fermi wave vectors for each detected pocket $k_{F\alpha} = 1.2(1) \times 10^{-2}$ Å^{-1}, $k_{F\beta} = 9.62(3) \times 10^{-2}$ Å^{-1}, and $k_{F\gamma} = 1.042(3) \times 10^{-1}$ Å^{-1}, where $k_F^2 = 2Fe/\hbar$.

Temperature-dependent dHvA oscillations are also observed, becoming obvious above 14 T in all temperatures [Fig. 3(a)] where the external magnetic field was kept perpendicular to the *ab* plane. Figure 3(b) presents background-free temperature-dependent dHvA oscillations ΔM versus inverse field $1/H$, where the smoothed background $\langle M \rangle$ is subtracted from the original oscillations M ($\Delta M = M - \langle M \rangle$). Similarly, an FFT is applied to the oscillation response ΔM and frequencies $F_\alpha, F_\beta, F_\gamma$ are identified while the amplitudes vary with temperature [Figs. 3(c)–3(f)]. Based on temperature factors R_T in the Lifshitz-Kosevich (LK) formula, amplitudes of FFT as a function of temperature could be used to evaluate the effective masses on each FS sheet [23],

$$R_T = \frac{\alpha m^* T/H}{\sinh(\alpha m^* T/H)}, \tag{4}$$

where $\alpha = 2\pi^2 K_B/e\hbar \approx 14.69$ T/K and $m^* = m/m_e$ is the effective mass of the cyclotron orbits. The effective masses are estimated for F_α to be $0.025(6)m_e$, and $0.110(5)m_e$, $0.112(3)m_e$ for F_β and F_γ, respectively. The small effective masses are consistent with a light mass of carriers in a Dirac semimetal. Moreover, a very small mass for the α FS pocket is comparable to a minute cyclotron mass in some other Dirac/Weyl semimetals such as LaAlGe, $ZrTe_5$, or α-Sn [24–26].

For insight into the topological character of the detected Fermi-surface sheets, LK formulas are applied to the background-free oscillation at 1.6 K with respect to inverse magnetic field (ΔM vs $1/H$) for both low- and high-frequency oscillation parts [Figs. 3(g) and 3(h)] [27–30],

$$\Delta M \propto -H^\lambda R_T R_D R_S \sin\left[2\pi\left(\frac{F}{H} - \gamma - \delta\right)\right], \tag{5}$$

where R_T is the temperature factor; $R_D = \exp(-\alpha m^* T_D/H)$ and $R_S = \cos(\pi g m^*/2)$ are field, spin-damping factors; $\alpha \approx 14.69$ T/K, mass ratio $m^* = m/m_e$, exponent λ is taken to be $1/2$ for 3D oscillations, and δ either $1/8$ or $-1/8$. For low frequency α [Fig. 3(g)] the fit gives $\gamma_\alpha = 0.0746(5)$. The γ is related to the Berry phase Φ_B by $\gamma = \frac{1}{2} - \frac{\phi}{2\pi}$, so calculations give $\Phi_\alpha = 0.851(1)\pi$. The calculations are consistent with a nontrivial $\pm\pi$, thus confirming a nontrivial topological character of the α Fermi-surface pocket. For high frequencies [Fig. 3(h)] $\gamma_\beta = 0.500(3)$, $\gamma_\gamma = 0.500(3)$, but also $\gamma_\beta = 0$, $\gamma_\gamma = 0$ fits are possible.

The Dingle temperature T_D is estimated by the temperature factor R_D in the LK fit. It is associated with the scattering rate τ of fast moving electrons caused by particle interactions and defects in the crystal. Its mathematical ex-

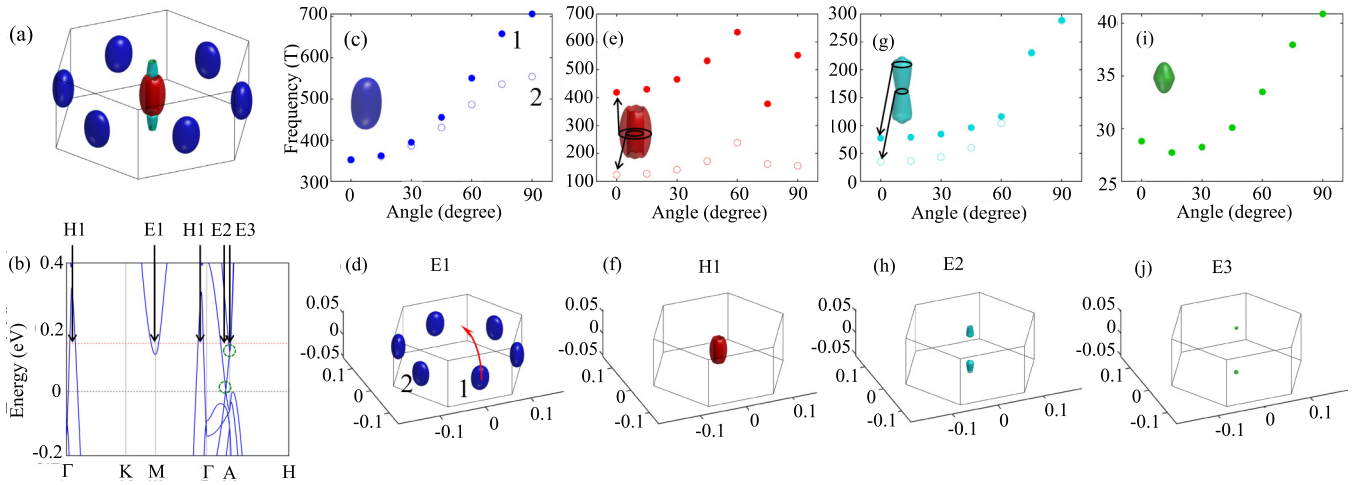

FIG. 4. (a) Theoretically calculated quantum oscillation frequencies for BaAuSb. (a) 3D Fermi-surface pockets for $E_F = 0.15$ eV and (b) the band structure near the Fermi level. At the Fermi energy, BaAuSb has three identical electron pockets $E1$–$E3$ and one hole pocket $H1$. The ellipselike hole pockets are related to M. The electron pocket is a Γ-centered hollow cylinder. The other two hole pockets are A centered. The green dashed circles indicate the position of Dirac points. Two types of Dirac-like crossings exist between the Γ-A and A points. (c)–(j) Angular dependence of quantum oscillation frequencies for particular parts of the Fermi surface. Solid and open symbols in (c) correspond to the different extremal orbits of cylindrical pockets at the edge of the Brillouin zone (d). Open symbols for the hole pocket $H1$ in (e) denote the outer orbit of the hollow cylinder depicted in the inset and in (f). Two different orbits are shown (g) for the dumbbell-like pocket [inset in (g), (h)] not detected by the quantum oscillation experiment. The smallest pocket (i), (j).

pression is $\tau = \frac{\hbar}{2\pi k_B T_D}$. The Dingle temperature for frequency α is $T_{D\alpha} = 2.28(1)$ K and the corresponding scattering rate is $\tau_\alpha = 5.33(2) \times 10^{-13}$ s. The calculation is almost ten times larger than those for high frequencies, whose $\tau_\beta = 5.8(3) \times 10^{-14}$ s, $\tau_\gamma = 1.4(2) \times 10^{-13}$ s with $T_{D\beta} = 21(1)$ K and $T_{D\gamma} = 9(1)$ K. A low Dingle temperature of the α pocket implies a large scattering rate and is consistent with a small scattering of nontrivial states at the Dirac cone in the reciprocal space. The mobilities are estimated based on the formula $\mu = \frac{e\tau}{m^*}$. They are $\mu_\alpha = 1.40(4) \times 10^4$ cm^2 V^{-1} s^{-1}, $\mu_\beta = 9.2(6) \times 10^2$ cm^2 V^{-1} s^{-1}, and $\mu_\gamma = 2.1(2) \times 10^3$ cm^2 V^{-1} s^{-1}. A very high μ_α mobility is consistent with a Dirac state.

We note that quantum oscillations detect three Fermi-surface pockets whereas Hall resistivity ρ_{xy} [Fig. 1(e)] is linear in magnetic field. This shows that electronic bands at the Fermi surface are likely compensated with similar overall electron and hole concentrations and with similar mobilities [31–33]. Interestingly, this is also the case for another *ABX*-type compound, LaAlGe, which is a type-II Weyl semimetal with tilted Weyl cones and an extremely small carrier mass [24,31,32,34]. It should also be noted that Fermi velocities in BaAuSb are similar to LaAlGe and are about three to ten times larger when compared to canonical Weyl semimetals NbP and WTe_2 [24,35,36].

Figure 4(a) presents a calculated Fermi surface of BaAuSb and associated quantum oscillation frequencies for the Fermi-level position at 0.15 eV [Fig. 1(b)] where the Fermi level cuts one hole (H) and three electron bands ($E1$–$E3$). At the edge of the Brillouin zone [Figs. 4(c) and 4(d)] there are three pairs of pockets, straight (1) and tilted (2), with different extremal orbits. The largest pocket at the zone center [Figs. 4(e) and 4(f)] has a hollow geometry, and the solid and open symbols correspond to the inner and outer orbit. Another elongated pocket in the zone center is dumbbell-like; its extremal orbits are depicted with open and solid symbols [Figs. 4(g) and 4(h)]. The smallest pocket at the zone center is closer to a sphere than an ellipse in reciprocal space; its angular evolution and shape are depicted in Figs. 4(i) and 4(j). From the frequency magnitudes and their angular evolution, the β and γ frequencies may come from the Γ-centered hollowlike pocket and from the pockets at the edge of the Brillouin zone with a trivial Berry phase ($H1$ and $E1$). The α frequency corresponds to a tiny pocket centered at the A point ($E3$) with a nontrivial Berry phase. We show detailed band structure information along the Γ-A line in Appendix C. From the calculation, the cyclotron effective masses in units of m_0 for zero angle are $H1 = 0.22$ (0.06 for the inner hollow orbit), $E1 = 0.41$, $E2 = 0.08$ (0.04 for the local maximum), and $E3 = 0.04$, all close to experimentally observed.

ARPES measurements confirm states near the Fermi surface (Fig. 5). There are states crossing the Fermi energy near the Γ point as well as flat bands at about 1.5 eV below the Fermi level. The experimental result [Figs. 5(a), 5(c), 5(e), and 5(g)] is in good agreement with calculations [Figs. 5(b), 5(d), 5(f), and 5(h)] for both $k_z = 0$ [Figs. 5(a)–5(d)] and $k_z = \pi/c$ [Figs. 5(e)–5(h)] planes. The k_F of holelike pockets around Γ is in good agreement with $k_{F\alpha}$ and $k_{F\beta}$ from quantum oscillations whereas the estimate of the calculated Fermi surface from quantum oscillations $S_{F\alpha}, S_{F\beta}$ agrees well with the 3.14×10^{-2} Å^{-2} ARPES Fermi surface near the Γ point [Fig. 5(c)].

Fermi velocities of BaAuSb trivial and nontrivial Fermi-surface pockets are comparable to Cd_3As_2 or graphene [37,38]. Of further interest is the creation of Weyl nodes by inducing magnetization in BaAuSb by magnetic atom substitution of deeply localized moments, such as Tm^{2+} or Eu^{2+}, or

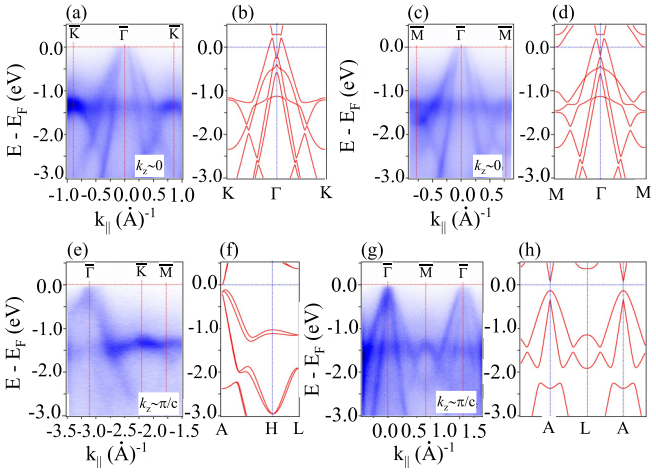

FIG. 5. Electronic band structure of BaAuSb acquired with ARPES. (a), (c) ARPES experimental band structure along the $\bar{K}$-$\bar{\Gamma}$-$\bar{K}$ and $\bar{M}$-$\bar{\Gamma}$-$\bar{M}$ directions within a momentum plane near $k_z \sim 0$, respectively. (b), (d) Calculated band structure along the K-Γ-K and M-Γ-M directions, respectively. (e), (g) ARPES experimental band structure along the $\bar{M}$-$\bar{K}$-$\bar{\Gamma}$ and $\bar{\Gamma}$-$\bar{M}$-$\bar{\Gamma}$ directions within a momentum plane near $k_z \sim \pi/c$, respectively. (f), (h) Calculated band structure along the H-L-A and A-L-A directions, respectively. For comparison with experimental results all calculated bands are shifted.

by the proximity effect. It should be noted that a ferromagnetic state above room temperature has been reported in thin films of Cd_3As_2 Dirac semimetal films grown on a ferromagnetic substrate [39].

III. CONCLUSION

In summary, our results show that BaAuSb features a mix of trivial and nontrivial 3D Fermi-surface pockets, but all with very large Fermi velocities and a small cyclotron mass. The masses are of the order of 1/10–1/100 of the bare electron mass resulting in very high mobility for the topologically nontrivial α pocket at the Brillouin zone center; the other 3D Fermi-surface pockets are likely compensated. The placement of magnetic divalent rare-earth atoms or proximization with magnetic layers may therefore split the Dirac points and generate a 3D Weyl semimetal state.

ACKNOWLEDGEMENTS

Work at Brookhaven National Laboratory was supported by U.S. DOE, Office of Science, Office of Basic Energy Sciences under Contract No. DE-SC0012704. Work at Renmin University was funded by the research Funds of Renmin University of China (RUC) (Grants No. 15XNLQ07, No. 18XNLG14, and No. 19XNLG17). A portion of this work was performed at the National High Magnetic Field Laboratory, which is supported by the National Science Foundation Cooperative Agreement No. DMR-1644779 and the State of Florida. B.Y. acknowledges funding from the European Research Council (ERC) under the European Union Horizon 2020 research and innovation programme (ERC Consolidator Grant NonlinearTopo, No. 815869). J.Z.M. was supported by the National Natural Science Foundation of China (12104379), and Guangdong Basic and Applied Basic Research Foundation (2021B1515130007). Y.H. and M.S. acknowledge the support from Swiss National Science Foundation under Grant No. 200021_188413.

APPENDIX A: METHODS

Single crystals of BaAuSb were grown by the high-temperature self-flux method. Small pieces of Ba, Au, and Sb lumps were mixed in an atomic ratio of 1:1:5. The mixture was placed in an alumina crucible, flushed with argon gas, and sealed in a quartz tube in vacuum. The ampoule was heated to 900 °C in a furnace, and kept over 24 h before a slow cooling over 10 days to 500 °C. Shiny crystals with a typical size of 2 mm × 2 × 0.5 mm were obtained after crystal decanting in a centrifuge. Extra residual Sb flux was cleaned by polishing before any measurements. The average stoichiometry was determined by the examination of multiple points on polished crystal surfaces using energy-dispersive x-ray spectroscopy (EDS) in a JEOL LSM-6500 scanning electron microscope. Electrical transport was measured by a conventional four-wire method in a Quantum Design PPMS-9T. Small cuboid specimens were taken to National High Magnetic Field Laboratory (NHMFL) for measurements of temperature- and angular-dependent de Haas–van Alphen (dHvA) oscillations in magnetic fields up to 35 T. Wide-angle x-ray scattering measurements were carried out in capillary transmission geometry at the 28-ID-1 beamline of the National Synchrotron Light Source II at Brookhaven National Laboratory. The setup utilized a 74.5-keV ($\lambda = 0.1665$ Å) x-ray beam. Two-dimensional diffraction data in the synchrotron experiment were integrated using the PYFAI software package [40]. The Rietveld analysis was carried out using the GSAS-II [41] software package.

For ARPES measurements, BaAuBi samples were cleaved *in situ* with a base pressure of better than 5×10^{-11} Torr. Regular angle-resolved photoemission (ARPES) measurements were performed at the ULTRA endstation of the Surface/Interface Spectroscopy (SIS) beamline of the Swiss

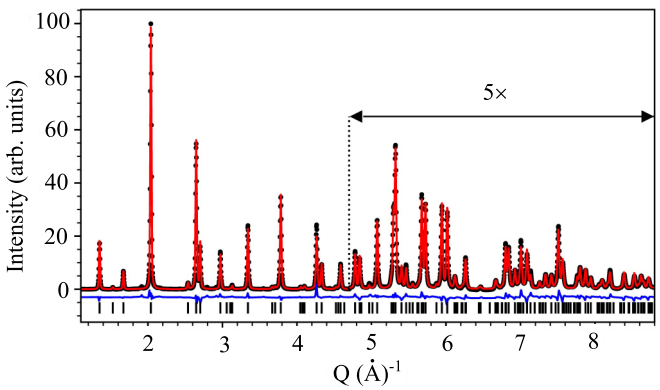

FIG. 6. Powder x-ray diffraction spectra of powdered BaAuSb crystal. Experimental data are shown by (○), the structural model is represented by the red solid line, and the difference curve (blue solid line) is offset for clarity. The vertical tick marks represent Bragg reflections of the $P6_3mmc$ space group.

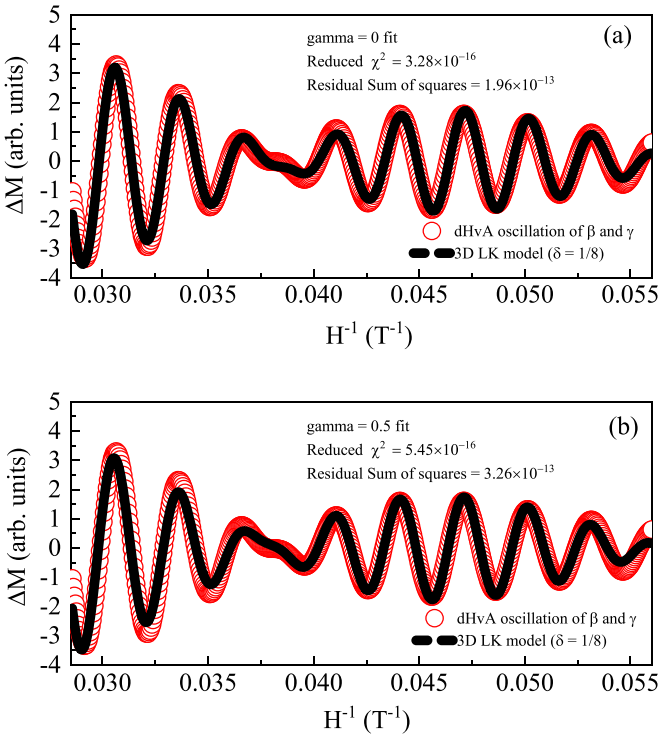

FIG. 7. Lifshitz-Kosevich fits for high frequencies β and γ for both (a) nontrivial and (b) trivial Berry phases.

Light Source using a Scienta-Omicron DA30L analyzer at 20 K. The energy and angular resolutions were set to 15–30 meV and 0.1°, respectively. The bar above the Brillouin zone point denotes point projection on the particular k.

First-principles calculations were performed using the density-functional theory (DFT) in the framework of the generalized gradient approximation [42] with the Vienna *ab initio* package [43]. From the whole first Brillouin zone band energy result we construct a Fermi-surface result. Based on the Fermi-surface result from the DFT calculation, we investigated the angle dependence of the Shubnikov–de Haas (SdH) frequencies in BaAuSb. We obtain the theoretical dHvA frequencies by the Onsager relation $F = (\Phi_0/2\pi^2)A$, where A is the extreme cross section of the corresponding Fermi pocket, $\Phi_0 = h/2e$ is the magnetic flux quantum, and h is the Planck constant. In calculations, we shifted the Fermi level to 0.15 eV to make a consistent result with the experiment.

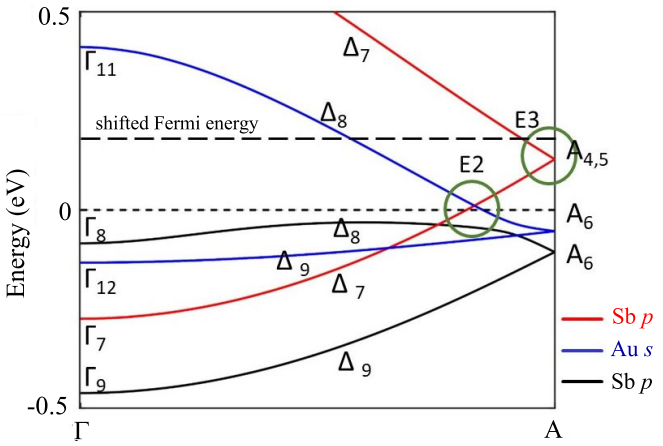

FIG. 8. The calculated band structure with band labels along the Γ-*A* line.

APPENDIX B: CHEMICAL COMPOSITION AND CRYSTAL STRUCTURE

An EDS analysis of crystals gives a Ba:Au ratio of 1.00(1):0.98(8):0.96(7), consistent with BaAuSb stoichiometry. The unit cell (Fig. 6) can be indexed in a $P6_3/mmc$ (194) space group with lattice parameters $a = b = 4.750(1)$Å, $c = 9.327(4)$Å and $\alpha = \beta = 90°$, $\gamma = 120°$, in agreement with the reported values [10]. Attempts to refine the occupancy for values smaller than the full occupancy of each atomic site did not improve the fit, indicating the absence of vacancy defects.

APPENDIX C: LIFSHITZ-KOSEVICH FITS

Whereas fits of small frequency α are possible only with a nontrivial Berry phase, i.e., only for $\gamma = 0.0746(5)$, in Fig. 7 we present fits of the multiband Lifshitz-Kosevich formula for high-frequency β and γ phases. For those frequencies, both trivial and nontrivial Berry phase fits are possible. However, first-principles calculations indicate a trivial Berry phase. It is not possible to establish that $E2$ pocket frequencies are present in the available data. W speculate that the absence is due to its low intensity below the noise floor and/or proximity to $E3$.

APPENDIX D: TYPE-1 DIRAC POINT AT *A*

Whereas Fig. 4(b) in the main text shows different parts of the band structure, in Fig. 8 we clearly show the type-1 Dirac point in BaAuSb at A.

[1] B. Yan and C. Felser, Topological materials: Weyl semimetals, Annu. Rev. Condens. Matter Phys. **8**, 337 (2017).

[2] T. O. Wehling, A. M. Black-Schaffer, and A. V. Balatsky, Dirac materials, Adv. Phys. **63**, 1 (2014).

[3] M. Z. Hasan and C. L. Kane, Colloquium: Topological insulators, Rev. Mod. Phys. **82**, 3045 (2010).

[4] H. Weyl, Gravitation and the electron, Proc. Natl. Acad. Sci. USA **15**, 323 (1929).

[5] X. Wan, A. M. Turner, A. Vishwanath, and S. Y. Savrasov, Topological semimetal and Fermi-arc surface states in the electronic structure of pyrochlore iridates, Phys. Rev. B **83**, 205101 (2011).

[6] E. J. Bergholtz, Z. Liu, M. Trescher, R. Moessner, and M. Udagawa, Topology and Interactions in a Frustrated Slab: Tuning from Weyl Semimetals to $\varepsilon > 1$ Fractional Chern Insulators, Phys. Rev. Lett. **114**, 016806 (2015).

[7] C.-L. Zhang, S.-Y. Xu, I. Belopolski, Z. Yuan, Z. Lin, B. Tong, G. Bian, N. Alidoust, C.-C. Lee, S.-M. Huang, T.-R. Chang, G. Chang, C.-H. Hsu, H.-T. Jeng, M. Neupane, D. S. Sanchez, H. Zheng, J. Wang, H. Lin, C. Zhang, H.-Z. Lu, S.-Q. Shen, T. Neupert, M. Z. Hasan, and S. Jia, Signatures of the Adler-Bell-Jackiw chiral anomaly in a Weyl fermion semimetal, Nat. Commun. **7**, 10735 (2016).

[8] B. Q. Lv, H. M. Weng, B. B. Fu, X. P. Wang, H. Miao, J. Ma, P. Richard, X. C. Huang, L. X. Zhao, G. F. Chen, Z. Fang, X. Dai, T. Qian, and H. Ding, Experimental Discovery of Weyl Semimetal TaAs, Phys. Rev. X **5**, 031013 (2015).

[9] H. Gao, J. W. F. Venderbos, Y. Kim, and A. M. Rappe, Topological semimetals from first principles, Annu. Rev. Mater. Res. **49**, 153 (2019).

[10] F. Merio, M. Pani, and M. L. Fornasini, RMX compounds formed by alkaline earths, europium and ytterbium—I. Ternary phases with M = Cu, Ag, Au; X = Sb, Bi, J. Less-Common Met. **166**, 319 (1990).

[11] B. Singh, S. Mardanya, C. Su, H. Lin, A. Agarwal, and A. Bansil, Spin-orbit coupling driven crossover from a starfruitlike nodal semimetal to Dirac and Weyl semimetal state in CaAuAs, Phys. Rev. B **98**, 085122 (2018).

[12] K. Nakayama, Z. Wang, D. Takane, S. Souma, Y. Kubota, Y. Nakata, C. Cacho, T. Kim, S. A. Ekahana, M. Shi, M. Kitamura, K. Horiba, H. Kumigashira, T. Takahashi, Y. Ando, and T. Sato, Observation of inverted band structure in the topological Dirac semimetal candidate CaAuAs, Phys. Rev. B **102**, 041104(R) (2020).

[13] Q. D. Gibson, L. M. Schoop, L. Muechler, L. S. Xie, M. Hirschberger, N. P. Ong, R. Car, and R. J. Cava, Three-dimensional Dirac semimetals: Design principles and predictions of new materials, Phys. Rev. B **91**, 205128 (2015).

[14] X. Zhang, Q. Liu, Q. Xu, X. Dai, and A. Zunger, Topological insulators versus topological Dirac semimetals in honeycomb vompounds, J. Am. Chem. Soc. **140**, 13687 (2018).

[15] J. Song, S. Kim, Y. Kim, H. Fu, J. Koo, Z. Wang, G. Lee, J. Lee, S. H. Oh, J. Bang, T. Matsushita, N. Wada, H. Ikegami, J. D. Denlinger, Y. H. Lee, B. Yan, Y. Kim, and S. W. Kim, Coexistence of Surface Superconducting and Three-Dimensional Topological Dirac States in Semimetal KZnBi, Phys. Rev. X **11**, 021065 (2021).

[16] J. Song, J. Wang, Y. Wang, L. Zhang, M. Song, Z. Li, L. Cao, D. Liu, and Y. Xiong, Kohler's rule and anisotropic Berry-phase effect in nodal-line semimetal ZrSiSe, J. Appl. Phys. **131**, 065106 (2022).

[17] R. Singha, A. K. Pariari, B. Satpati, and P. Mandala, Large nonsaturating magnetoresistance and signature of nondegenerate Dirac nodes in ZrSiS, Proc. Natl. Acad. Sci. USA **114**, 2468 (2017).

[18] Y.-F. Huang, W.-L. Zhu, Y.-Y. Wang, Q.-X. Dong, L.-B. Zhang, C.-S. Li, H. OuYang, Z.-A. Ren, and G.-F. Chen, Large unsaturated transverse and negative longitudinal magnetoresistance in the compensated semimetal $MoGe_2$, Phys. Rev. B **103**, 134116 (2021).

[19] M. B. T. Tchokonté, J. J. Mboukam, A. K. H. Bashir, B. M. Sondezi, K. R. Kumar, A. M. Strydom, and D. Kaczorowski, Electrical resistivity and thermodynamic properties of the ferromagnet Nd_2Pt_2In, J. Alloys. Comp. **753**, 41 (2018).

[20] A. Tari, *The Specific Heat of Matter at Low Temperatures* (Imperial College Press, London, 2003).

[21] D. Mandrus, B. C. Sales, and R. Jin, Localized vibrational mode analysis of the resistivity and specific heat of LaB_6, Phys. Rev. B **64**, 012302 (2001).

[22] J. Stakiewicz, M. Evangelisti, and Z. Fisk, Specific heat of $Nd_{1-x}Ca_xB_6$ single crystals, Phys. Rev. B **83**, 113108 (2011).

[23] D. Shoenberg, *Magnetic Oscillations in Metals* (Cambridge University Press, Cambridge, UK, 2009).

[24] Z. Hu, Q. Du, Y. Liu, D. Graf, and C. Petrovic, High Fermi velocities and small cyclotron masses in LaAlGe, Appl. Phys. Lett. **117**, 222410 (2020).

[25] G. Zheng, J. Lu, X. Zhu, W. Ning, Y. Han, H. Zhang, J. Zhang, C. Xi, J. Yang, H. Du, K. Yang, Y. Zhang, and M. Tian, Transport evidence for the three-dimensional Dirac semimetal phase in $ZrTe_5$, Phys. Rev. B **93**, 115414 (2016).

[26] L. D. Anh, K. Takase, T. Chiba, Y. Kota, K. Takiguchi, and M. Tanaka, Elemental topological Dirac semimetal α-Sn with high quantum mobility, Adv. Mater. **33**, 2170404 (2021).

[27] J. Hu, Z. Tang, J. Liu, X. Liu, Y. Zhu, D. Graf, K. Myhro, S. Tran, C. N. Lau, J. Wei, and Z. Mao, Evidence of Topological Nodal-Line Fermions in ZrSiSe and ZrSiTe, Phys. Rev. Lett. **117**, 016602 (2016).

[28] J. Hu, J. Y. Liu, D. Graf, S. M. A. Radmanesh, D. J. Adams, A. Chuang, Y. Wang, I. Chiorescu, J. Wei, L. Spinu, and Z. Q. Mao, π Berry phase and Zeeman splitting of Weyl semimetal TaP, Sci. Rep. **6**, 18674 (2016).

[29] J. Hu, Z. Tang, J. Liu, Y. Zhu, J. Wei, and Z. Mao, Nearly massless Dirac fermions and strong Zeeman splitting in the nodal-line semimetal ZrSiS probed by de Haas–van Alphen quantum oscillations, Phys. Rev. B **96**, 045127 (2017).

[30] S. Xu, J.-F. Zhang, Y.-Y. Wang, L.-L. Sun, H. Wang, Y. Su, X.-Y. Wang, K. Liu, and T.-L. Xia, Shubnikov–de Haas and de Haas–van Alphen oscillations in the topological semimetal $CaAl_4$, Phys. Rev. B **99**, 115138 (2019).

[31] G. Chang, B. Singh, S.-Y. Xu, G. Bian, S.-M. Huang, C.-H. Hsu, I. Belopolski, N. Alidoust, D. S. Sanchez, H. Zheng, H. Lu, X. Zhang, Y. Bian, T.-R. Chang, H.-T. Jeng, A. Bansil, H. Hsu, S. Jia, T. Neupert, H. Lin, and M. Z. Hasan, Magnetic and noncentrosymmetric Weyl fermion semimetals in the RAlGe family of compounds (R = rare earth, Phys. Rev. B **97**, 041104(R) (2018).

[32] S.-Y. Xu, N. Alidoust, G. Chang, H. Lu, B. Singh, I. Belopolski, D. S. Sanchez, X. Zhang, G. Bian, H. Zheng, M.-A. Husanu, Y. Bian, S.-M. Huang, C.-H. Hsu, T.-R. Chang, H.-T. Jeng, A. Bansil, T. Neupert, V. N. Strocov, H. Lin, S. Jia, and M. Z. Hasan, Discovery of Lorentz-violating type II Weyl fermions in LaAlGe, Sci. Adv. **3**, e1603266 (2017).

[33] Q. Wang, Q. Yin, and H. Lei, Magnetotransport properties of compensated semimetal HfB_2 with high-density light carriers, J. Phys.: Condens. Matter **32**, 015601 (2020).

[34] M. Udagawa and E. J. Bergholtz, Field-Selective Anomaly and Chiral Mode Reversal in Type-II Weyl Materials, Phys. Rev. Lett. **117**, 086401 (2016).

[35] P. Li, Y. Wen, X. He, Q. Zhang, C. Xia, Z.-M. Yu, S. A. Yang, Z. Zhu, H. N. Alshareef, and X.-X. Zhang, Evidence for topological type-II Weyl semimetal WTe_2, Nat. Commun. **8**, 2150 (2017).

[36] Z. Wang, Y. Zheng, Z. Shen, Y. Lu, H. Fang, F. Sheng, Y. Zhou, X. Yang, Y. Li, C. Feng, and Z.-A. Xu, Helicity-protected

ultrahigh mobility Weyl fermions in NbP, Phys. Rev. B **93**, 121112(R) (2016).

[37] M. Neupane, S.-Y. Xu, R. Sankar, N. Alidoust, G. Bian, C. Liu, I. Belopolski, T.-R. Chang, H.-T. Jeng, H. Lin, A. Bansil, F. Chou, and M. Z. Hasan, Observation of a three-dimensional topological Dirac semimetal phase in high-mobility Cd_3As_2, Nat. Commun. **5**, 3786 (2014).

[38] Z. Jiao and H. J. V. Zandvliet, Determination of the Fermi velocity of graphene on MoS_2 using dual mode scanning tunneling spectroscopy, Appl. Phys. Lett. **118**, 163103 (2021).

[39] M. Uchida, T. Koretsune, S. Sato, M. Kriener, Y. Nakazawa, S. Nishihaya, Y. Taguchi, R. Arita, and M. Kawasaki, Ferromagnetic state above room temperature in a proximitized topological Dirac semimetal, Phys. Rev. B **100**, 245148 (2019).

[40] V. Kieffer, V. Valls, N. Blanc, and C. Hennig, New tools for calibrating diffraction setups, J. Synchrotron Radiat. **27**, 558 (2020).

[41] B. H. Toby and R. B. V. Dreele, GSAS-II: The genesis of a modern open-source all purpose crystallography software package, J. Appl. Crystallogr. **46**, 544 (2013).

[42] J. P. Perdew, K. Burke, and M. Ernzerhof, Generalized Gradient Approximation Made Simple, Phys. Rev. Lett. **77**, 3865 (1996).

[43] G. Kresse and D. Joubert, From ultrasoft pseudopotentials to the projector augmented-wave method, Phys. Rev. B **59**, 1758 (1999).